

A home-made portable device based on Arduino Uno for pulsed magnetic resonance of NV centers in diamond

Cite as: AIP Advances **12**, 065321 (2022); <https://doi.org/10.1063/5.0089161>

Submitted: 06 April 2022 • Accepted: 07 June 2022 • Published Online: 24 June 2022

 G. Mariani, A. Umemoto and  S. Nomura



View Online



Export Citation



CrossMark

ARTICLES YOU MAY BE INTERESTED IN

[A microfabricated fiber-integrated diamond magnetometer with ensemble nitrogen-vacancy centers](#)

Applied Physics Letters **120**, 191104 (2022); <https://doi.org/10.1063/5.0089732>

[Broadband, large-area microwave antenna for optically detected magnetic resonance of nitrogen-vacancy centers in diamond](#)

Review of Scientific Instruments **87**, 053904 (2016); <https://doi.org/10.1063/1.4952418>

[Nanotesla sensitivity magnetic field sensing using a compact diamond nitrogen-vacancy magnetometer](#)

Applied Physics Letters **114**, 231103 (2019); <https://doi.org/10.1063/1.5095241>

Read Now!

AIP Advances

Materials Science Collection

A home-made portable device based on Arduino Uno for pulsed magnetic resonance of NV centers in diamond

Cite as: AIP Advances 12, 065321 (2022); doi: 10.1063/5.0089161

Submitted: 6 April 2022 • Accepted: 7 June 2022 •

Published Online: 24 June 2022



View Online



Export Citation



CrossMark

G. Mariani,^{a)} A. Umemoto, and S. Nomura

AFFILIATIONS

Division of Physics, University of Tsukuba, Tennodai 1-1-1, Ibaraki 305-8571, Japan

^{a)}Author to whom correspondence should be addressed: mariani.giacomo.wp@alumni.tsukuba.ac.jp

ABSTRACT

We describe the realization of a homemade and portable setup to perform experiments of pulsed magnetic resonance of nitrogen-vacancy (NV) centers in diamonds. The system is fully implemented by using an Arduino Uno board equipped with an AVR microcontroller that is used as a transistor-transistor logic pulse sequencer to drive precise laser and microwave pulses with a resolution of 62.5 ns. The equipment is assembled with low-cost modules on a printed circuit board and placed in a compact box with a volume of $20 \times 40 \times 10 \text{ cm}^3$. The detection system is based on a switched integrator and a photodiode in the vicinity of a diamond substrate and read by oversampling the analog-to-digital converter of Arduino Uno. We characterize a CVD diamond sample by performing the pulsed optically detected magnetic resonance and we show the possibility to perform a coherent manipulation of the electron spin of NV centers by driving Rabi oscillations up to 6 MHz with microwave powers within 1 W. We demonstrate different pulse sequences to study electron spin relaxation and dephasing. Finally, we propose additional modules and an antenna to perform the multifrequency manipulation of the electron spin by microwave and radio-frequency pulses. Compared to the previous studies, our system results in a low-cost setup with significantly reduced complexity, which finds application as a learning module for science education and enables a wider audience to access the magnetic resonance in diamond.

© 2022 Author(s). All article content, except where otherwise noted, is licensed under a Creative Commons Attribution (CC BY) license (<http://creativecommons.org/licenses/by/4.0/>). <https://doi.org/10.1063/5.0089161>

I. INTRODUCTION

Nitrogen-vacancy (NV) centers are point defects constituted by a nitrogen atom and an adjacent vacancy in the diamond lattice. The state of the electron spin of NV centers can be controlled by means of laser and microwave (MW) pulses at room temperature, making it a robust platform for sensing or implementing quantum protocols. The experimental setups to perform measurements of magnetic resonance with NV centers are mostly based on bulky tabletop setups.^{1–4} As the technological requirements for the control NV center at room temperature have been consolidated, the tabletop setups are gradually turning into more compact and portable magnetometers. Fully CMOS-integrated systems⁵ and diamond samples integrated with an optical fiber^{6,7} have been developed. In other systems with a handheld sensing head, the diamond sample is directly placed in the vicinity of a photodiode (PD).^{8–12} However, the previous devices require large investments and specialized technical

skills that restrict the magnetic resonance in diamonds to research laboratories.

Microcontrollers (MCUs) offer a simple solution to implement complex pulse sequences, which find application in scientific research.¹³ Among MCUs, the Arduino Due microcontroller has been widely used in nuclear magnetic resonance (NMR) spectrometers as a pulse sequencer^{14,15} and has been recently used for a low-frequency modulation of the magnetic resonance in NV centers in diamonds.¹⁶ MCUs alone or combined with software defined radio (SDR) systems¹⁷ have been demonstrated as a low-cost and less complicated alternative to field-programmable gate arrays (FPGAs)¹⁸ to implement pulse sequences for experiments of magnetic resonance. Here, we report the construction of a homemade and portable setup to perform measurements of pulsed magnetic resonance of NV centers in diamond. Compared to the previous studies, we employ an Arduino Uno board equipped with an AVR microcontroller and a 16 MHz crystal to directly implement

pulse sequences with a single clock precision of 62.5 ns. We choose the Uno board for the minimal complexity of the programming environment and for the ready-to-use open source libraries to interface Arduino Uno with various devices. Our complete equipment is assembled in a portable and compact box with a weight of 1.8 kg, by combining low-cost discrete modules on breakout boards, which are mostly commercially available on e-commerce markets. Our system finds an immediate application in teaching laboratories of academia^{19,20} but it may also be adopted in research and industry. We discuss the capabilities of our system by performing a characterization of a CVD diamond sample containing NV centers. We demonstrate Arduino Uno as a transistor-transistor logic (TTL) pulse sequencer to coherently drive the electron spin of NV centers.

II. MICROCONTROLLER-BASED SETUP

NV centers in diamonds possess an electron spin-triplet ground state with a zero-field splitting (ZFS) transition centered at 2870 MHz at room temperature. The electron spin of NV centers can be optically initialized by a laser pulse with a wavelength of 520 nm, which preferentially polarizes the spin in the low $m_s = 0$ state through the inter-system crossing transition to its metastable state. The state of the electronic spin is read out by another laser pulse, which induces the photoluminescence (PL) from NV centers

in a spectral range of 600–800 nm. Microwave (MW) pulses in resonance with the ground state transitions produce a change in the PL through which the spin state is probed. The degeneracy of the $m_s = \pm 1$ states can be lifted by the Zeeman effect, applying an external static magnetic field. The Zeeman splitting is proportional to $\Delta f = 2\gamma_e B_0$, where $\gamma_e = 28$ MHz/mT is the electron gyromagnetic ratio and B_0 is a static magnetic field aligned along one of the NV center's directions. The dynamics of the electronic spin are in the scale of microseconds; thus, a precise synchronization of the MW and laser pulses with sub- μ s granularity is required.

Figure 1(a) shows a picture of the portable setup. The parts are secured on a perforated aluminum sheet and placed in a box with the size of $20 \times 40 \times 10$ cm³. At the heart of our system, there is the Arduino Uno development board that we use to control the surrounding printed circuit board (PCB) modules for the generation of laser and MW pulses and the detection of the PL from NV centers. The system operates with three low-power AC/DC adapters with DC output voltages of 6 V (6 W), 12 V (6 W), and 15 V (7.5 W), which supply the MW elements, laser driver, and detection modules, respectively. A personal computer connected with a universal serial bus (USB) cable to the box is minimally required to load the programming code on the Arduino board and read the measured data from the serial port. The parts to assemble the setup are listed in Appendix C. Various elements are either commercially available breakout boards or home-designed using the EasyEDA software²¹

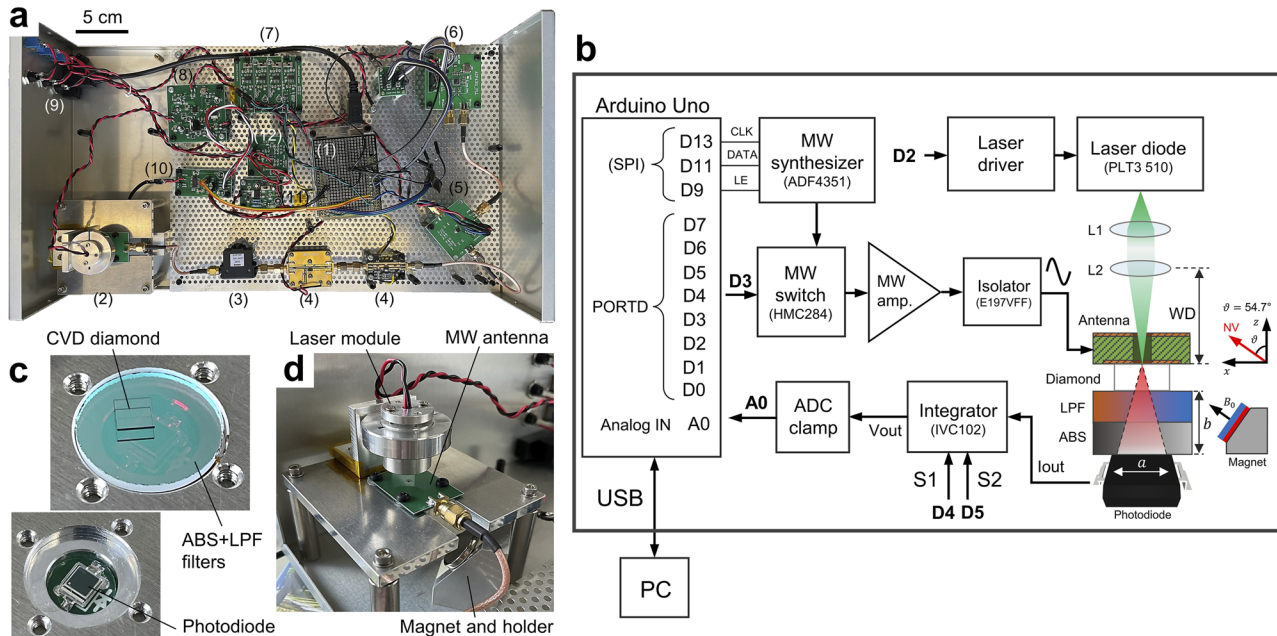


FIG. 1. (a) Interior of the experimental setup: (1) Arduino Uno, (2) sample holder, (3) MW isolator, (4) MW amplifiers, (5) MW switch, (6) MW synthesizer, (7) 5, 3.3 V voltage regulators, (8) laser driver, (9) input of AC/DC converters and USB, (10) switched integrator, (11) ADC clamp, and (12) integrator's ± 12 V regulator. (b) Schematic of the setup. The Arduino board controls the modules by using the digital pins D2–D5, D9, D11, and D13. The laser beam is collimated by a lens (L1) and focused by a lens (L2), with a working distance WD = 16 mm from the surface of the diamond. The distance between the diamond and the photodiode (PD) is $b = 2$ mm. The active area of the PD is $a^2 = 2.65 \times 2.65$ mm². (c) Sample holder. The diamond sample with a size of $3 \times 3 \times 0.25$ mm³ is placed on the top of the reflective (LPF) and the absorptive glass (ABS) filters. The PD mounted on a PCB is placed on the back side of the filters and fixed to the aluminum plate with screws. (d) Attachment of the MW antenna and alignment system of the laser diode on the sample holder.

and manufactured by the surface mount (SMT) assembly service of the JLCPBCB (Shenzhen JIALICHUANG Electronic Technology Development Co., Ltd.) company. A simplified schematic of the setup with the connections to Arduino Uno is shown in Fig. 1(b).

A. Optical excitation and detection

The excitation and read-out of the electron spin state of NV centers are performed by a laser diode (PLT3 510, Osram) with a wavelength of 520 nm and a maximum power of 10 mW. The laser beam is collimated by a plastic aspheric lens L1 (CAY033, Thorlabs) and focused by a second aspheric lens L2 (CAX183, Thorlabs). As shown in Fig. 1(d), the laser diode and the lenses are inserted in an aluminum cylinder secured in a collar and attached to an angle bracket for the alignment over the sample. The details of the laser diode module are described in the [supplementary material](#). A home-built laser driver receives the TTL from the digital pin D2 of Arduino and produces current regulated pulses that are sent to the laser diode. The laser driver is constituted by a current source based on an op-amp and a MOSFET, as described in [Appendix A](#). We performed the measurements with the laser power in a range of 3–5 mW.

To lift the degeneracy of the electron spin, we applied a static magnetic field by a neodymium disk magnet with a diameter of 20 mm and a thickness of 3 mm, attached to an aluminum inclined block for the alignment to the [111] direction of NV centers, as shown in Fig. 1(d).

The photoluminescence from NV centers is detected by a Si photodiode (PD) used in the photovoltaic mode. To find a compromise between the fastest response in a condition of zero bias and a sufficient collection efficiency we chose a surface-mount PD (BPW34S-Z, Osram) with a low junction capacitance and an active area of $a^2 = 2.65 \times 2.65 \text{ mm}^2$, where a is the side of the photosensitive area of the PD. We chose a surface-mount PD soldered on a PCB to avoid the interference of the common T0-5 metal cans with the static magnetic field applied to NV centers. The PCB with the PD is fixed with screws to a custom aluminum plate. The details of the plate are described in the [supplementary material](#). As shown in Fig. 1(c), an absorptive long-pass filter (RG630, Schott) followed by a reflective long-pass filter (5CGA-630, Newport) is placed in a stack on the surface of the PD. To realize a compact detection module and ensure a sufficient collection efficiency, the diamond substrate is placed directly on the surface of the top filter at a distance of $b = 2 \text{ mm}$ from the surface of PD.

B. Microwave excitation

The manipulation of the electron spin of NV centers is performed by using a MW synthesizer, switch, and amplifiers, which are low-cost breakout boards operating at the supply voltage of 5 or 3.3 V. The MW synthesizer is based on the ADF4351 (Analog Devices), a MW phase-locked loop (PLL) with an output frequency in a range of 25–4400 MHz, a fundamental mode of the voltage-controlled oscillator (VCO) in a range of 2200–4400 MHz, and a phase noise of -90 dBc/Hz at an offset of 20 kHz from a central frequency of 3.3 GHz. The frequency range of the ADF4351 is compatible with the MW resonance transitions of NV centers. The registers of the ADF4351 are programmed with Arduino Uno by SPI communication using the digital pins D9, D11, and D13. We use voltage dividers to interface the 5 V logic of Arduino with the

3 V logic of the synthesizer. The ADF4351 has four programmable output powers ranging from -4 to $+5 \text{ dBm}$.

The MW pulses are generated by a MW switch controlled by the digital pin D3 of Arduino. We designed the PCB module of the MW switch based on the HMC284AMS8G (Analog Devices), an SPDT non-reflective switch that provides a fast switch time of 20–30 ns and high isolation $>45 \text{ dB}$ from both its output ports at 3 GHz. The switch is driven with a dual inverter 74HCT2G04 (NXP) to obtain the MW signal with logic high on the output port RF2, which has higher isolation. After the MW switch, the MW pulses pass through a two-stage amplification.

The first stage is a low noise amplifier (LNA) constituted by a 9 dB gain LNA (SPF5189, Quorvo) or a 20 dB gain LNA (TQP3M9009, Quorvo). The second stage is a driver amplifier (TQP7M9103, Quorvo) to reach a maximum output power of about 28 dBm (0.631 W). The power supplies of the MW elements are provided by the 6 V AC/DC converter, which feeds three 5 V low-dropout (LDO) regulators (ADM7150, Analog Devices) and a 3.3 V LDO (ADM7160, Analog Devices) that are used to power the two MW amplifiers, the switch, and the synthesizer, respectively. The amplifiers and the ADF4351 sufficiently cover a wide range of MW powers. Fixed attenuators or digital programmable attenuators, such as the PE4302 module (pSemi), could be used for a fine-tuning the output power. The MW pulses are sent to a MW antenna that generates a homogeneous MW field across the diamond sample. To block unwanted reflections to the MW amplifier, we inserted a 1 W RF isolator (E197VFF, MTC—Microwave Technology Corporation) with a frequency range of 2700–3100 MHz before the antenna.

To coherently drive the spin ensemble, we designed a MW loop antenna similar to the one presented in Ref. 22. Our antenna was fabricated on a FR-4 PCB with a size of $25 \times 33.5 \text{ mm}^2$, a thickness of 0.6 mm, and a $35 \mu\text{m}$ thick Cu foil. The front side of the PCB is constituted by a planar loop-gap resonator with an external diameter of 17.4 mm, an inner through-hole with a diameter of 1 mm, a gap with a width of 0.15 mm, a feed line with a width of 0.13 mm, and a length of 8 mm. The back side of the PCB is fully covered with a Cu foil and constitutes the ground plane. As shown in Fig. 1(d), the antenna is attached to the sample holder with screws, with the front side toward the diamond surface and the ground plane upward.

In a similar configuration used in Ref. 23, the laser beam passes through the hole in the PCB to reach the diamond substrate, which is sandwiched between the antenna and the optical filters. The resonance mode of the antenna generates a spatially homogeneous magnetic field oriented along the z -axis across the hole. Our antenna has a resonance frequency of 2740 MHz and a quality factor of $Q = 24$, as shown in Fig. 3(b), and a Rabi frequency gain of $\sim 6.9 \text{ MHz}/\sqrt{\text{W}}$ measured at a frequency of 2742.2 MHz, as shown in Fig. 4(h). The antenna, designed to efficiently drive the [111] transition at MW powers within 1 W, is compatible with the detection bandwidth of the Arduino Uno.

C. TTL sequence and detection

Arduino Uno is equipped with the ATmega328 microcontroller and a crystal with a frequency of 16 MHz. The TTL sequence to synchronize the devices and implement pulse sequences is generated by the digital pins of Arduino Uno. The fast port manipulation of the digital pins can be performed using simple low-level instructions,²⁴

with timing as short as 1 clock of the crystal (62.5 ns), as shown in Figs. 2(b) and 2(c). We used the second register PORTD of Arduino Uno's port D, which simultaneously controls the digital pins D0–D7 by using Boolean operations to create the TTL pulses, as shown in Fig. 1(b). For more details about the instructions for the port manipulation, we refer the reader to the [supplementary material](#).

A scheme of the TTL sequence to measure the electron spin state of NV centers is shown in Fig. 2(a). A cycle of the sequence is composed of a laser pulse, which serves for both initialization and read-out of the electronic spin, a waiting time τ_a to complete the spin polarization, a MW pulse for the spin manipulation, and a delay τ_b between consecutive cycles set to adjust the response of the MW switch. For the measurements, we used a laser pulse duration of 8 μs , $\tau_a = 1 \mu\text{s}$, and $\tau_b = 62.5 \text{ ns}$. The photoluminescence emitted by NV centers produces a photocurrent in the photodiode that is integrated by a precision switched integrator (IVC102, Blown Blurr).²⁵ The measurements of the magnetic resonance of NV centers may also be performed in a continuous mode by setting a constant TTL voltage for the MW switch and laser driver during the integration time of the integrator. As shown in Fig. 2(e), the IVC102, controlled by Arduino through two switches S1 and S2, integrates the photocurrent in an internal capacitor with $C = 100 \text{ pF}$. A cycle is repeated thousands of times, and the pulsed photocurrent $I_{PD}(t)$ is continuously integrated by the IVC102. When S1 is set low, the integration starts and it stops after an integration time T equal to the total time of the repeated cycles, as shown in Fig. 2(d). The output voltage set by the capacitor is given by

$$V_{out} = \frac{1}{C} \int_0^T I_{PD}(t) dt. \quad (1)$$

A second integration is repeated without the MW pulses to normalize the voltage and to compensate for temporal fluctuations of the laser diode. The measurements are repeated 100 times for averaging and to increase the signal-to-noise ratio. The IVC102 is installed on a custom PCB, taking particular care in guarding traces and shielded cables to avoid current leakage to the input pins. The IVC102 is supplied by a low-noise regulator (LTC3260, Analog Devices) installed on a custom PCB, which generates an output voltage of $\pm 12 \text{ V}$ from the 15 V AC/DC converter. The output voltage of the IVC102 is clamped to the ground and to $\sim 4.8 \text{ V}$, set by an LM317 regulator, with two Schottky diodes to protect the analog-to-digital converter (ADC) of Arduino from over/under voltages.

The output voltage of the IVC102 is fed to the analog pin A0 of Arduino and read during the hold time of the IVC102 by the built-in 10-bit ADC of Arduino. During the time S1 is held high, the voltage developed in the IVC102 should not exceed 200 mV for accurate readings. Arduino Uno takes 13 ADC clock cycles to perform the analog-to-digital conversion. The ADC clock speed is calculated from the crystal frequency of 16 MHz divided by a prescaler factor F , which results in a time for a single reading equal to $T_{ADC} = 0.8125 F \mu\text{s}$. For a faster acquisition during the hold cycle, we wrote a low prescaler factor of 32 into the ADCSRA register of the Arduino ADC, which reduces the *analogRead* (A0) time to $T_{ADC} = 26 \mu\text{s}$ per sample without degrading the resolution of the measurement. As

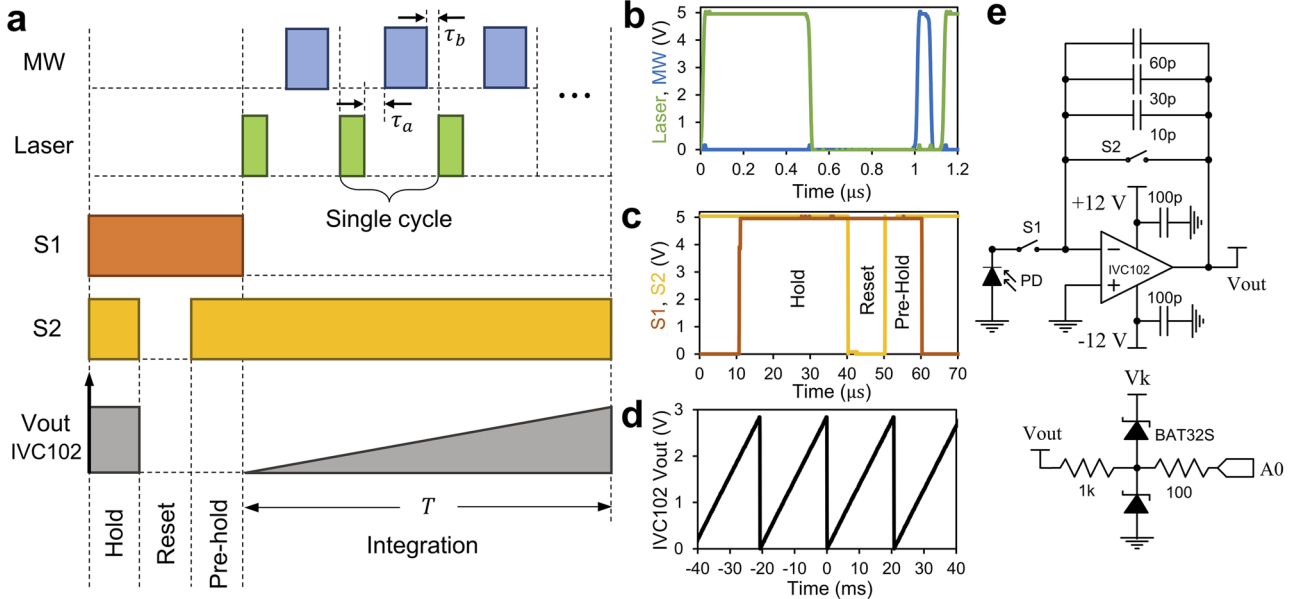


FIG. 2. (a) Schematic of the TTL sequence for the initialization, manipulation, and detection of NV centers. (b)–(d) Example of TTL pulses generated by Arduino Uno and output voltage of the integrator acquired by an oscilloscope. (b) Shortest MW pulse (blue line) and delay time τ_b of 62.5 ns, with a laser pulse (green line) and delay τ_a of 0.5 μs . (c) Control pulses to the S1 and S2 switches of the IVC102 integrator for a single ADC reading during the hold interval. A logic high (low) corresponds to the switch open (close). (d) Example of the output voltage of the IVC102 integrator for an integration time of $T = 20 \text{ ms}$. (e) Schematic of the IVC102 and protection circuit of the Arduino ADC with $V_k \sim 4.8 \text{ V}$ adjusted by using an LM317 regulator.

shown in Fig. 2(c), we measured a time of $\sim 30 \mu\text{s}$ for one reading during the hold time. The typical contrast of a normalized magnetic resonance spectrum of NV centers is in the order of 1%. To obtain a larger resolution from the Arduino ADC, we used an oversampling and decimation technique where the signal is oversampled 4ⁿ times during the hold time to get n extra bits of resolution.²⁶ To perform our measurements, we oversampled 256 times the voltage at the output of the IVC102 to obtain an effective resolution of 14 bit from the ADC. We tested the ADC with the previous settings by measuring different voltages from a source meter (2602A, Keithley). We confirmed that the linearity of the ADC is ensured in a range of 0–4.95 V, with the Arduino board powered from USB. We chose a reset and pre-hold period of 10 μs for the IVC102, as recommended by the producer. It should be noted that, in our case, the output voltage of the IVC102 contained a 50 Hz noise line that could be effectively suppressed by using integration times longer than ~ 20 ms.

III. CHARACTERIZATION OF THE ELECTRON SPIN PROPERTIES

To demonstrate our system, we measured the NV centers contained in a (001) single crystal CVD type IIa diamond substrate (ElementSix), with a size of $3 \times 3 \times 0.25 \text{ mm}^3$ and nitrogen concentration $< 1 \text{ ppm}$. The diamond chip was annealed at a temperature of 1000° for 2 h and treated with acids.

We first performed a pulsed optically detected magnetic resonance (ODMR) of NV centers. Figures 3(a) and 3(b) show the ODMR measured at a MW pulse duration of 2 μs . We measured the zero-field spectrum in Fig. 3(a) and with an arbitrary alignment of the static magnetic field B_0 with respect to the NV axis in Fig. 3(b), respectively. In the latter, we resolved eight resonance peaks, which correspond to the four directions of NV centers in the diamond lattice for the transitions between $m_s = 0$ and $m_s = \pm 1$ states. We further resolved the splitting given by the hyperfine interaction with the ^{14}N nuclear spin, determined by the longitudinal component of the coupling constant $A_{||} \approx -2.16 \text{ MHz}$. The splitting of each peak was well resolved at the MW power of 0 dBm, as shown in the inset of Fig. 3(b). The asymmetry in the contrast of the ODMR spectrum

with respect to the ZFS is due to the resonance frequency of the MW loop antenna set at 2740 MHz, as shown by the $|S11|$ parameter measured by the network analyzer in Fig. 3(c).

To confirm the possibility to drive precise MW pulses, we measured the Rabi oscillations of the electron spin at MW powers in a range of 13.9–28.1 dBm. The Rabi oscillations were probed by driving MW pulses with increasing duration at a fixed MW frequency and normalized by the same sequence without MW pulses, as shown in Fig. 4(a). We first aligned B_0 along the [111] direction of NV centers at a central frequency of 2742.2 MHz close to the resonance of the antenna, as shown in Fig. 4(b). Then, we measured the Rabi oscillations at a zero detuning for increasing MW power P_{MW} , as shown in Figs. 4(c)–4(g). Figure 4(h) shows the linear dependence of the Rabi frequency Ω with respect to the square root of the MW power as $\Omega/2\pi \propto \gamma_e \sqrt{P_{\text{MW}}}$. We measured a maximum Rabi frequency of 5.8 MHz at a maximum MW power of 28.1 dBm, which is compatible with the maximum detectable Rabi frequency of 8 MHz by using Arduino Uno.

We characterized the longitudinal relaxation T_1 of the electron spin by using a common-mode rejection method,^{27,28} as shown in Fig. 5(a). After the initialization pulse into the $m_s = 0$ state, a MW π -pulse flips the spin into the $m_s = -1$ state. The MW pulse is followed by a delay time τ during which the spin relaxation occurs. The data are normalized by applying the same sequence without the MW π -pulse. The signal is proportional to the residual spin polarization of the NV centers excited by the MW π -pulse. The MW frequency is set in resonance with the [111] transition. The measurement is well fit by a stretched exponential decay $1 + A \exp[-(t/T_1)^\beta]$, where the fit parameters are the amplitude A , the decay time T_1 , and the stretched exponential parameter β with a value between 0 and 1. The β parameter describes the distribution of relaxation times of a large ensemble of NV centers. We obtained a relaxation time of $T_1 = 292 \pm 6 \mu\text{s}$ and a parameter of $\beta = 0.7$.

We measured the coherence of the electron spin by applying the Ramsey and Hahn echo sequence, as shown in Fig. 5(b). Figure 5(c) shows the free-induction decay (FID) of the electron spin, with the MW frequency in resonance with the [111] transition. The data show damped oscillations at a frequency equal to the detuning of

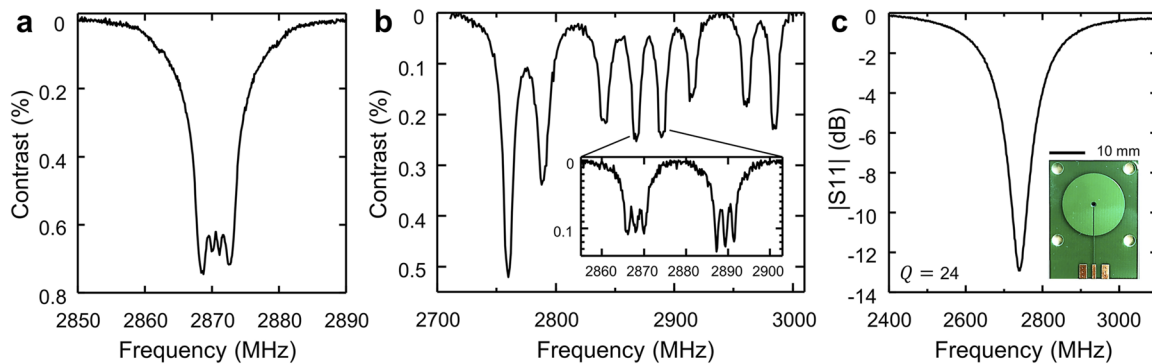
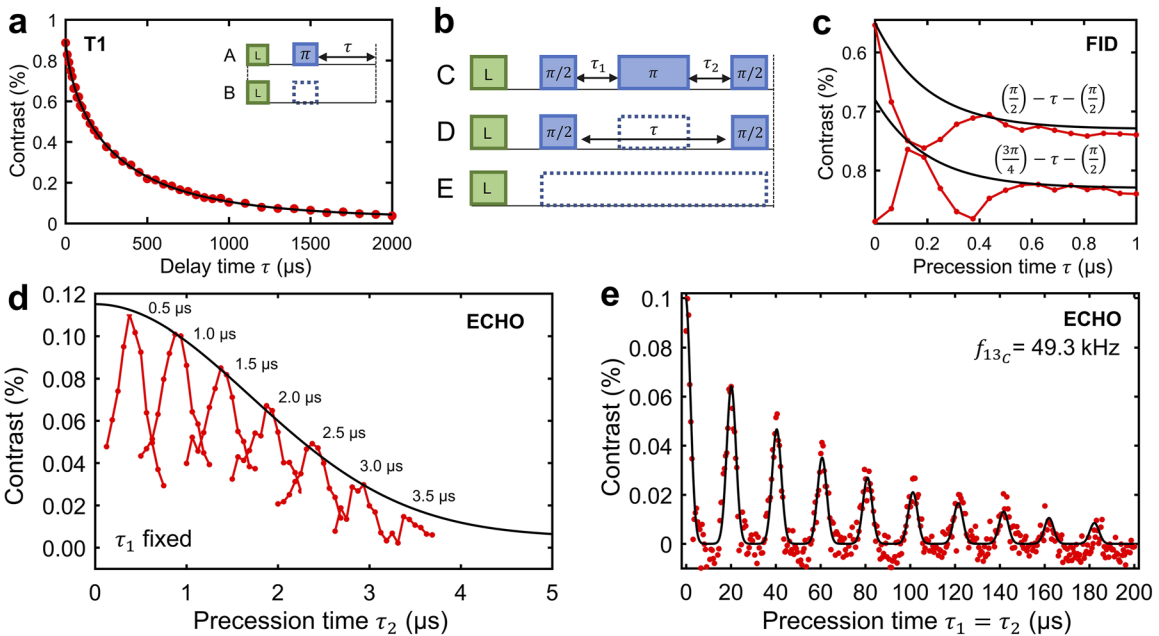
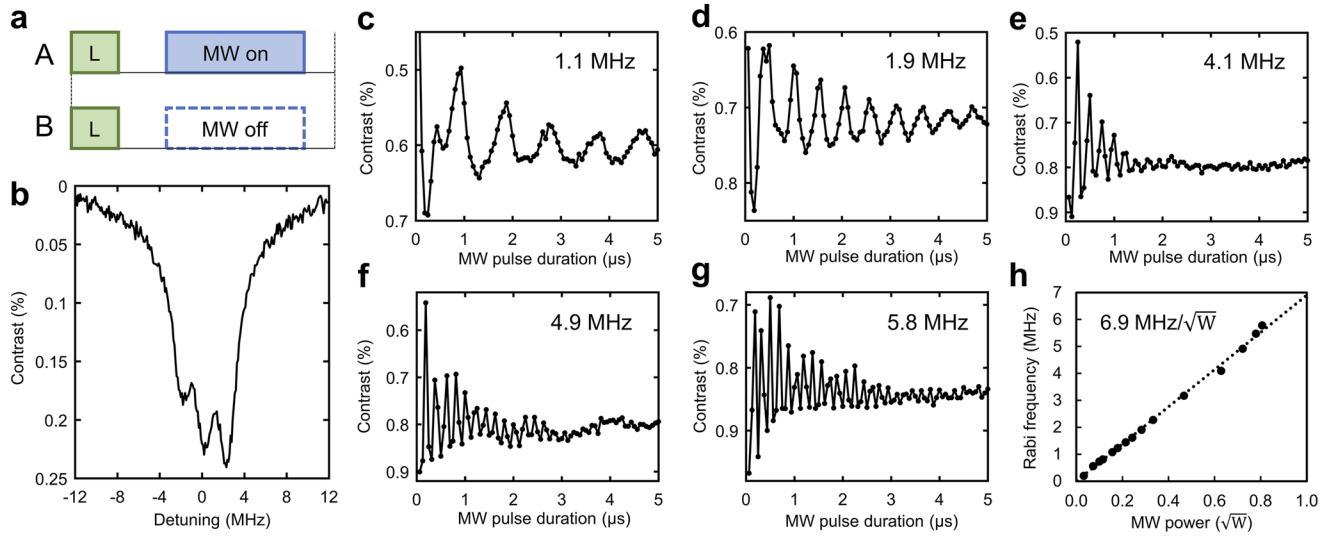


FIG. 3. Pulsed optically detected magnetic resonance (ODMR) of NV centers: (a) $B_0 = 0$, MW power of -9 dBm , and step of 0.1 MHz. (b) Arbitrary alignment of B_0 , MW power of 9 dBm , and step of 1 MHz. The inset shows the splitting due to the hyperfine interaction with the ^{14}N nuclear spin, resolved at the MW power of 0 dBm, with the step of 0.2 MHz. MW pulses have a duration of 2 μs . (c) Measured $|S11|$ parameter of the MW loop antenna shown in the inset. The antenna is fabricated on a FR-4 PCB with a size of $25 \times 33.5 \text{ mm}^2$ and a thickness of 0.6 mm.



~ 2.2 MHz due to the ^{14}N hyperfine coupling, with exponential decay of the amplitude with time constant $T_2^* \sim 0.2$ μs . In type IIa diamonds, the decoherence of the electron spin is caused by the coupling with the surrounding spin bath formed by ^{13}C nuclear spins. The diamond lattice is mainly constituted by spinless ^{12}C isotopes and by the 1.1% of a natural abundance of ^{13}C isotopes that have a nuclear spin with a Larmor precession frequency determined by the gyromagnetic ratio $\gamma_{^{13}\text{C}} = 10.705$ kHz/mT. The coupling between the electron spin of NV centers and the proximal ^{13}C causes a collapse and revival of the spin-echo signal at a rate equal to the Larmor frequency of the ^{13}C nuclear spin.²⁹ As shown in Fig. 5(d), we observed an electron spin decoherence with a Gaussian decay with a time constant of 2.4 μs , measured from the single echoes of the electron spin. For large delays, we observed a collapse and revival of the electron spin-echo, as shown in Fig. 5(e). At the resonance transition, we estimated a magnetic field of $B_0 \simeq \Delta B/\gamma_e = 4.56$ mT that was nearly aligned parallel to the [111] direction. From B_0 , we estimated a precession frequency of the ^{13}C nuclear spin equal to 48.8 kHz, in agreement with the 49.4 kHz extracted from the data in Fig. 5(e). The amplitude of the revivals had an exponential decay with the form of

$A \exp[(2\tau_{1,2}/T_2)^\beta]$ with $\beta = 0.78$ and $T_2 = 115 \pm 9$ μs . The spin-echo sequence was normalized with respect to the FID sequence to eliminate the drift of the spin relaxation and minimize the effect of inaccurate MW pulses. The short coherence time is similar to previously reported values for spin ensembles in CVD samples with $N < 1$ ppm³⁰ and is attributed to a misalignment of the external static magnetic field of a few degrees.³¹

IV. MULTIFREQUENCY EXCITATION

The presented setup is sufficient to characterize the electron spin properties of NV centers in diamonds by using laser and MW pulses. The system is versatile and can perform various measurements by adding discrete modules on PCB, controlled by Arduino Uno.

We describe the incorporation of additional modules that can be used to perform experiments of multifrequency manipulation of the electron spin by MW and RF pulses. The spatial inhomogeneities and the random fluctuations of the MW field over the spin ensemble limit the time of the spin manipulation. A weak longitudinal

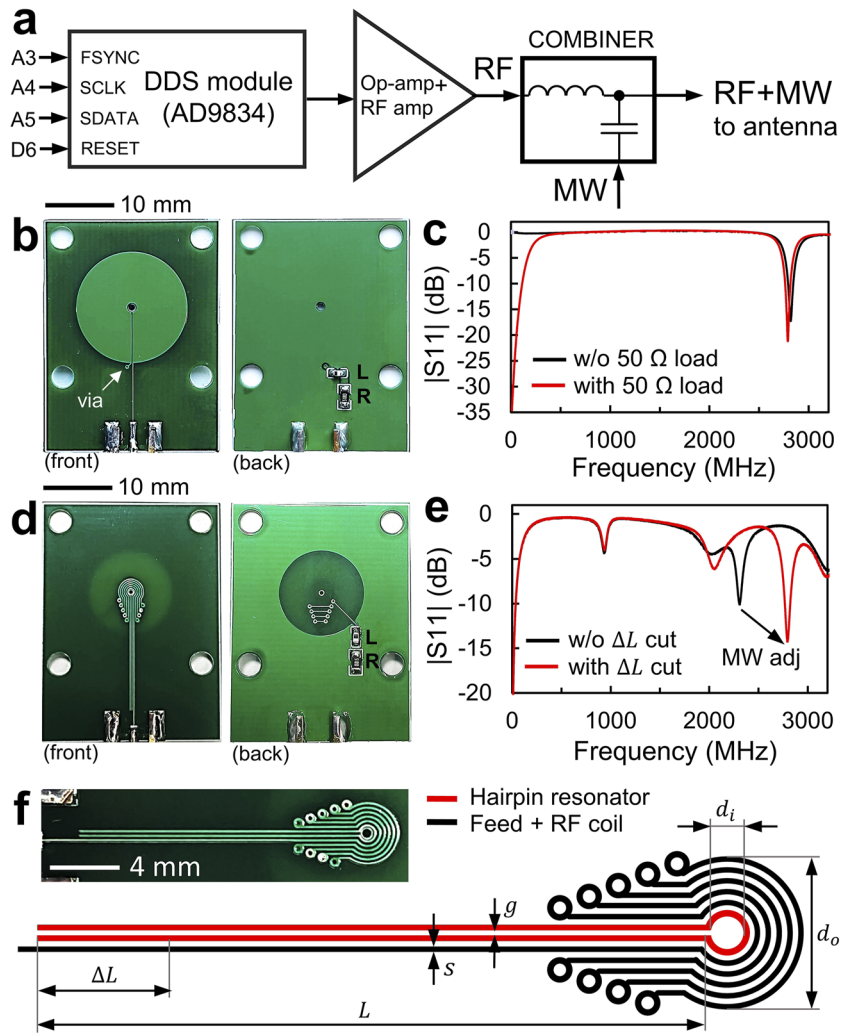


FIG. 6. (a) Schematic of the modules used for the multifrequency excitation. (b) MW loop antenna modified for the RF excitation and (c) measured $|S_{11}|$. (d) MW/RF antenna used for the experiment of multifrequency excitation. The antennas in (b) and (d) are fabricated on an FR-4 PCB with a size of 25×33.5 mm 2 and a thickness of 0.6 mm. (e) Measured $|S_{11}|$ of the MW/RF antenna and adjustment of the MW resonance frequency by cutting the resonator. (f) Enlarged view and schematic (on scale) of the MW/RF antenna, constituted by a hairpin resonator and a spiral RF coil connected to the feed line. All the traces s and gaps g have a width of 0.13 mm. The hairpin resonator has an inner diameter $d_i = 0.8$ mm and a half-length $L = 16$ mm. The MW resonance frequency is adjusted by a cutting a length $\Delta L \approx 3.2$ mm of the resonator's extremes. The outer diameter of the MW/RF antenna is $d_o = 3.66$ mm. The antennas use terminations with $L = 56$ nH and $R = 50\ \Omega$.

radio-frequency (RF) field at a frequency near the Rabi frequency of the electron spin can be used to protect the spin from decoherence by creating doubly dressed states.^{32–35} This method is similar to the concatenated continuous driving (CCD) technique, in which the amplitude or phase modulation of the MW pulses is effective to decouple the spin from the noise of the MW source.^{36–38}

Here, the RF field is generated by a direct digital synthesizer (DDS) module (AD9834, Analog Devices), supplied by a 5 V low-dropout (LDO) regulators (ADM7150, Analog Devices) connected to the 6 V AC/DC converter. As shown in Fig. 6(a), the output frequency ω_{RF} and phase φ_{RF} of the RF field are programmed by using the digital pins A3-A5 of the Arduino board. The DDS is triggered through its external RESET pin connected to the digital pin D6 of the Arduino board. The amplitude of the RF field is controlled and amplified by an external op-amp (OPA353UA, Texas Instruments) and an LNA (SPF5189, Quorvo), as described in Appendix B. Then, the RF and MW fields are combined by using an LC combiner and fed to an antenna. In previous studies of multifrequency excitation, the fields were commonly fed to coplanar waveguides, thin wires or patterned traces terminated with a $50\ \Omega$ load, to drive single electron spins with magnetic fields of high intensity while achieving the same spatial distribution.^{32,33,39–42} However, in the case of a spin ensemble, thin wires increase the spatial inhomogeneities and require a precise alignment of the laser beam at a few micrometers from the wire. Instead, a current loop is suitable for generating homogeneous magnetic fields in a wide area.

We propose a MW/RF antenna specifically designed for experiments of multifrequency excitation with a spin ensemble, which uses a bichromatic homogeneous magnetic field generated at the center of a loop resonator. As a first attempt, we modified the MW loop antenna shown in Fig. 3(b). We added a via, connecting the edge of the antenna to a surface-mount device (SMD) 56 nH choke inductor on the back side of the PCB and then to an SMD $50\ \Omega$ resistor to the ground, as shown in Fig. 6(b). This time we used an external diameter of 17 mm for the loop-gap to compensate for the shift of the resonance frequency. In this condition, similarly to an omega loop resonator inserted in a transmission line,⁴³ the RF field can be fed to the antenna without a significant alteration of the MW resonance mode and frequency, as shown in Fig. 6(c). The antenna has a resonance frequency of 2789 MHz, a quality factor of $Q = 26$, and a cut-off (-6 dB) frequency of 154 MHz. We obtained a Rabi frequency gain of $\sim 5.9\text{ MHz}/\sqrt{\text{W}}$ at a MW frequency of 2781.4 MHz and a gain of $\sim 0.5\text{ MHz}/\sqrt{\text{W}}$ at an RF of 2 MHz, experimentally calculated from the first and second order Rabi frequencies Ω_1 and Ω_2 of the electron spin.

To obtain higher gains of the AC fields, we realized a MW/RF antenna constituted by a MW resonator included in an RF coil on a 0.6 mm thick PCB, as schematized in Fig. 6(f). All the patterns are realized by using traces and gaps with a minimum width of $s = g = 0.13\text{ mm}$, limited by the accuracy of manufacturing, to realize the most compact structure. The MW resonator is a U-shaped or hairpin resonator with a total length of $\sim 34.5\text{ mm}$ and a loop with an inner diameter of $d_i = 0.8\text{ mm}$ located at the half-length. The MW is inductively coupled by using a feed line adjacent to the resonator. The same feed line is also used for the RF excitation and is wrapped around the hairpin resonator in a five-turn spiral coil, connecting the turns on the back side of the PCB through vias, as shown in Fig. 6(d).

The coil is terminated to the ground by an SMD 56 nH inductor and an SMD $50\ \Omega$ resistor on the back side of the PCB.

Compared to the first configuration shown in Fig. 6(b), we obtained higher AC magnetic fields at the center of the through-hole. The MW magnetic field is increased by reducing the diameter of the inner loop at the cost of lower spatial uniformity. The RF magnetic field at the center of the spiral coil $B_{RF} \propto [N/(d_o - d_i^*)] \ln(d_o/d_i^*)$, with $d_i^* = d_i + 2(s+g)$ and d_o inner and outer diameters of the coil, respectively, is increased by the larger number of turns $N = 5$ in the smallest area. Another advantage of the MW/RF antenna is the possibility to adjust the MW resonance frequency by reducing the length of the hairpin resonator, cutting its extremes for a length ΔL , as indicated in Fig. 6(f). The thin traces were removed by using a box cutter, and the shift of the MW resonance peak was monitored with a network analyzer, as shown in Fig. 6(e). The adjusted MW/RF antenna with a cut of $\Delta L \simeq 3.2\text{ mm}$ has a resonance frequency of 2794 MHz, a quality factor of $Q = 17$, and a cut-off (-6 dB) frequency of 63 MHz. We obtained a gain of $\sim 14\text{ MHz}/\sqrt{\text{W}}$ at the MW frequency of 2782.1 MHz and a gain of $\sim 4.0\text{ MHz}/\sqrt{\text{W}}$ at the RF of 2 MHz. The calculated RF gain is equivalent to a magnetic field gain for the parallel component of the RF field equal to $B_{\parallel}/I_{AC} = 1.01\text{ mT/A}$, which is similar to the gain $B_{\parallel}/I_{AC} = 1.04\text{ mT/A}$ measured for an RF microcoil proposed for NV centers in Ref. 44. Compared to PCB antennas of previous studies, the obtained Rabi frequency gain at MW frequency is higher than the gain of $\sim 4.6\text{ MHz}/\sqrt{\text{W}}$ of the ring antenna of Ref. 22 and lower than the gain of $\sim 22.1\text{ MHz}/\sqrt{\text{W}}$ of the double split-ring antenna of Ref. 45. The advantage of our antenna is the possibility to drive a homogeneous bichromatic field for a spin ensemble. Compared to Ref. 44, where a separated RF microcoil and MW coplanar waveguide are used, our antenna is robust, easy to handle, and suitable for compact detection systems. Compared to thin wires, the inhomogeneities of the field are reduced and the difficulty of aligning the laser spot near the wire is reduced.

To protect the spin from decoherence, we are interested in the longitudinal component of the RF field $B_{RF,\parallel}$ and the transverse component of the MW field $B_{MW,\perp}$ with respect to the NV axis.^{32,33} In the frame of the NV axis, the spin dynamics can be described by the following Hamiltonian in the first interaction picture (1P):

$$H^{1P} = \left[\frac{\Omega_1 + \delta\Omega_1(t)}{2} \right] \sigma_x + [\Omega_2 + \delta\Omega_2(t)] \cos(\omega_{RF}t + \varphi_{RF}) \sigma_z + C^{2H} [\Omega_2 + \delta\Omega_2(t)] \cos(2\omega_{RF}t + \varphi_{RF}) + \frac{\delta_b(t)}{2} \sigma_z, \quad (2)$$

where $\sigma_{x,z}$ are the Pauli matrices for the $1/2$ spin, with $\omega_{RF} \ll \omega_{MW}$ and $\Omega_2 < \Omega_1$. In Eq. (2), we neglect the Bloch–Siebert shift given by the transverse component of the RF field $B_{RF,\perp}$. The first- and second-order Rabi frequency are $\Omega_1 = \Omega_{MW,\perp}$ and $\Omega_2 = \Omega_{RF,\parallel}$, respectively. The RF field has frequency ω_{RF} and phase φ_{RF} , taking $t = 0$ as the starting point of the MW pulse. In Eq. (2), we included the component at the second-harmonic of the RF source, where C^{2H} is the ratio with respect to the fundamental mode. The noise of the sources and the magnetic noise are indicated by $\delta\Omega_{1,2}$ and δ_b , respectively. The protection of the electron spin is effective when $\omega_{RF} \sim \Omega_1$ and for the near frequencies.

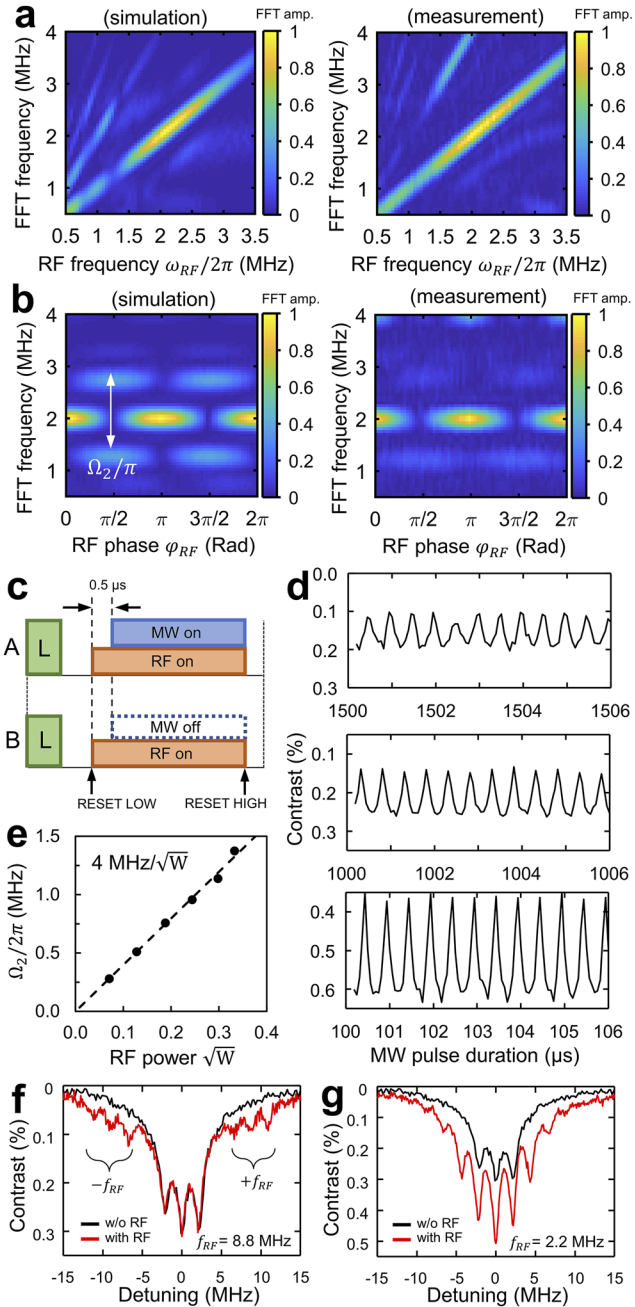


FIG. 7. Multifrequency excitation of the electron spin. FFT of the Rabi oscillations for a MW/RF pulse duration of 0.125–6.125 μs with a step of 62.5 ns, $\Omega_1/2\pi = 2$ MHz. Taking $\Omega_2/2\pi = 0.758$ MHz: (a) variable RF with $\varphi_{RF} = 0$ and (b) variable RF phase, with $\omega_{RF} = \Omega_1$. The FFTs are obtained from a Hanning window and a zero-filling of the data to show smoother curves. (c) Normalization A/B for the measurements of multifrequency excitation. (d) Rabi oscillations at $\Omega_2/2\pi = 0.785$ MHz, $\varphi_{RF} = 0$ for MW/RF pulse durations of 100, 1000, and 1500 μs . (e) Measurement of Ω_2 as a function of the square root of the RF power fed to the MW/RF antenna. (f) and (g) ODMR of the [111] resonance transition centered at a MW frequency of 2789.1 MHz by using a strong RF field and a weak MW field with a pulse duration of 4 μs . The amplitudes of the fields are $\Omega_2/2\pi = 1.36$ MHz and $\Omega_1/2\pi = 0.14$ MHz with $\omega_{RF}/2\pi$ equal to (f) 8.8 MHz and (g) 2.2 MHz.

The measurements were performed by using a common-mode rejection pulse sequence in which the signal is normalized by taking the pulse sequence with or without the MW pulse with the RF pulse always present, as shown in Fig. 7(c). The DDS was triggered 0.5 μs before the MW pulse; this allowed the DDS to settle and to precisely adjust the initial phase of the RF field. We set the MW frequency on resonance with the $m_s = -1$ transition with the static magnetic field aligned along the NV axis. We studied the evolution of the electron spin for an RF field with variable phase and frequency with $\Omega_1/2\pi = 2$ MHz at a MW power of 13 dBm and an RF power of 15.5 dBm. Figure 7(a) shows the FFT of the Rabi oscillations as a function of the RF for $\varphi_{RF} = 0$. For $\omega_{RF} \sim \Omega_1$, the spin is locked at the RF and protected from decoherence. Figure 7(b) shows the FFT as a function of the RF phase for $\omega_{RF} = \Omega_1$. For $\varphi_{RF} = 0, \pi$, the spin is driven at the first-order Rabi frequency Ω_1 , whereas, for $\varphi_{RF} = \pi/2, 3\pi/4$, the spin is driven at the frequencies $\Omega_1 \pm \Omega_2$, originating from the second-order Rabi frequency. From the data, we measured $\Omega_2/2\pi = 0.758$ MHz. The simulations performed by solving the Lindblad master equation and Eq. (2) show a good agreement with the experimental data and previous studies.^{33,46} The noise contributions were described by using an Ornstein–Uhlenbeck (OU) process. The remaining inconsistencies were attributed to a possible spatial field gradient that was not considered in the simulation.

The choice of the RF phase is crucial to control the decay and the change in the amplitude of the Rabi oscillations.^{34,46} An RF field with $\varphi_{RF} = 0, \pi$, in-phase or 180° out of phase with the Rabi oscillations, effectively drives the electron spin without the beating caused by Ω_2 . We measured the Rabi oscillations for $\varphi_{RF} = 0$ at longer MW/RF pulse durations, as shown in Fig. 7(d). We extended the Rabi oscillations at a frequency of 2 MHz with a MW pulse duration beyond 1500 μs , accompanied by a decrease in contrast and amplitude of the oscillations for increasing duration. Compared to the single driving shown in Fig. 4, the decay of the Rabi oscillations is now ultimately limited by the longitudinal relaxation of the electron spin at T_1 . At a MW pulse of around 2000 μs , the amplitude and contrast of the oscillations are further reduced in agreement with the data in Fig. 5(a). The coherence protection of the spin ensemble's Rabi oscillations finds application to build robust quantum protocols for quantum information.⁴⁷ The 90° out of phase $\varphi_{RF} = \pi/2, 3\pi/4$ measurement reveals the second-order Rabi frequency $\Omega_2/2\pi = \gamma_e B_{RF,\parallel}$, from which we quantitatively derived the amplitude of the longitudinal RF field. We measured Ω_2 for different RF powers, from which we determined the RF gain of $\sim 4 \text{ MHz}/\sqrt{W}$ of the MW/RF antenna, as shown in Fig. 7(e).

To confirm the nature of the double dressing, we measured the ODMR spectrum for the [111] direction by applying a strong RF field with $\Omega_2 \gg \Omega_1$ and probing the spectrum with a weak MW field. We analyzed the case of $\Omega_2/2\pi = 1.36$ MHz and $\Omega_1/2\pi = 0.14$ MHz. As shown in Fig. 7(f), by applying an RF field with a frequency of 8.8 MHz, we observed sidebands at a frequency shift of $\pm \omega_{RF}$ with respect to the resonance transition. These sidebands are new energy levels created by modulation with the longitudinal RF field and are a signature of the double dressing of the spin transition.^{32,33,42,48,49} The sidebands have been proved useful for several applications, such as the heterodyne detection of RF fields,⁴² zero-field level anti-crossing,⁴⁹ or sensing of RF fields.⁵⁰ As shown in Fig. 7(g), the choice of an RF field with a frequency of 2.2 MHz near the ^{14}N hyperfine splitting leads to an overlapping of the energy

levels in the ODMR spectrum and the maximum contrast increases about 1.6 times. A higher contrast is beneficial to obtain a higher sensitivity for DC magnetometry similar to a multi-tone excitation by a modulated MW field^{51,52} but without the need of an RF mixer and with the possibility to control independently the MW and RF fields to optimize the signal. For the case studied in Fig. 7(g), an integration time of 15.6 ms with an average of 100 repetitions gives a normalized contrast error of about 0.004%, which results in an error of about 10 kHz on the position of the central peak extracted by a fit with a Lorentzian envelope. When sensing a magnetic field from a DC current, to reduce the measurement time, a second combiner with a MOSFET to feed and switch the current may also be used together with the double driving to obtain a modulated signal at the maximum slope of the ODMR peak.

Finally, we evaluated the DC gain of the MW/RF antenna by measuring the shift of the [111] peak of the ODMR spectrum when a regulated DC current is applied to the combiner instead of the AC signal, as shown in Fig. 8. Figure 8(a) shows an example of the

ODMR shift in condition of zero bias and by applying a DC current of 5 mA. The ODMR peaks are fitted with a Lorentzian envelope, and the magnetic field is derived from the average frequency shift of the three peaks originating from the hyperfine splitting. As shown in Fig. 8(b), a DC gain equal to $B_{\parallel}/I_{DC} = 1.44 \mu\text{T}/\text{mA}$ is obtained for the parallel component of the magnetic field, which is near the AC gain derived from the dressed states of electron spin.

V. CONCLUSIONS

We constructed a homemade and portable device to perform experiments of pulsed magnetic resonance with NV centers in diamond, based on the Arduino Uno board. We demonstrated the electron spin manipulation of NV centers by using synchronized pulse sequences generated from the microcontroller with a resolution of 62.5 ns. We characterized a CVD diamond sample showing the possibility to measure the pulsed ODMR spectrum, Rabi oscillations, and relaxation and dephasing of the electron spin. Our setup was realized by using inexpensive mass-produced commercial modules on PCB and interfaced with the Arduino Uno board by using open-source libraries.

By introducing a few additional modules on PCB, we demonstrated experiments of multifrequency excitation of the electron spin by MW and RF pulses. We designed a MW/RF antenna, which combines an RF coil with a MW resonator, to simultaneously drive the spin with a bichromatic field. The planar structure of the antenna is suitable for compact detection systems, where it is not possible to insert a large three-dimensional RF coil. We measured a Rabi frequency gain of $4 \text{ MHz}/\sqrt{\text{W}}$ at an RF of 2 MHz, calculated from the second-order dressed state of the electron spin. We tested our antenna to conduct various measurements of multifrequency excitation, such as the electron spin protection, RF field sensing, and generation of sidebands.

The simplicity and low cost of the excitation and detection modules and the open-source programming environment of Arduino Uno make our setup more accessible to a non-specialized audience and suitable as a learning module for experiments of magnetic resonance in schools.

SUPPLEMENTARY MATERIAL

See the [supplementary material](#) for the technical drawings of the sample holder, laser module, and an introduction of the programming code.

ACKNOWLEDGMENTS

The authors would like to thank Hong Liu for providing the financial support necessary for the realization of this project. The authors would like to thank Dr. H. Watanabe, who provided us the vector network analyzer used to characterize the microwave devices of the manuscript.

AUTHOR DECLARATIONS

Conflict of Interest

The authors have no conflicts to disclose.

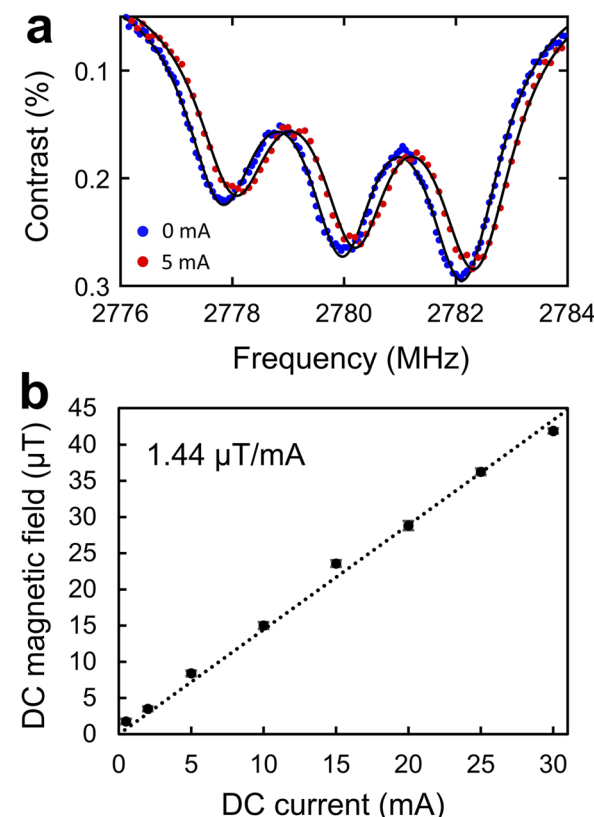


FIG. 8. DC gain of the MW/RF antenna. (a) [111] peak of the ODMR spectrum measured at a MW power of -9.2 dBm in conditions of zero DC current (blue points) and with a DC current of 5 mA (red points). The black line is fit with three Lorentzian envelopes centered at each peak position. (b) DC magnetic field extracted from the shift of the ODMR peak as a function of the applied current. The error bars are calculated from the error of the fit and noise of the normalized signal in a range of $0.32\text{--}0.63 \mu\text{T}$ for about 300 repetitions of the pulsed signal integrated for about 22.1 ms. A laser pulse of $8 \mu\text{s}$, a wait time of $1 \mu\text{s}$, and MW pulse of $4 \mu\text{s}$ were used.

Author Contributions

G. Mariani: Conceptualization (equal); Investigation (equal).
A. Umemoto: Investigation (equal). **S. Nomura:** Supervision (equal).

DATA AVAILABILITY

The data that support the findings of this study are available from the corresponding author upon reasonable request.

APPENDIX A: LASER DRIVER

The laser driver is designed to drive low-power laser diodes <100 mA and is realized with SMD components on a custom-built

PCB board. The laser driver is a common current regulated source based on an operational amplifier and a MOSFET. Figure 9 shows the schematic of the laser driver, which is powered by the 12 V AC/DC converter.

The voltage is regulated to V_{reg} by the adjustable LM317 regulator with a soft-start circuit, which provides a source of current for the laser diode, as shown in Fig. 9(a). As shown in Fig. 9(c), a rail-to-rail op-amp (OPA353UA, Texas Instruments) is connected to the gate of a MOSFET to provide the current regulation. The op-amp has enough gain to force the MOSFET to maintain the output at the same voltage V_{ref} applied to the non-inverting input. A precise current regulation is determined by the voltage drop V_{ref} across a sense resistor $R_s = 22 \Omega$ as $I_{reg} = V_{ref}/R_s$. As shown in Fig. 9(d), the reference voltage V_{ref} is provided by a precision reference circuit (REF3425, Texas Instruments) and adjusted by using a

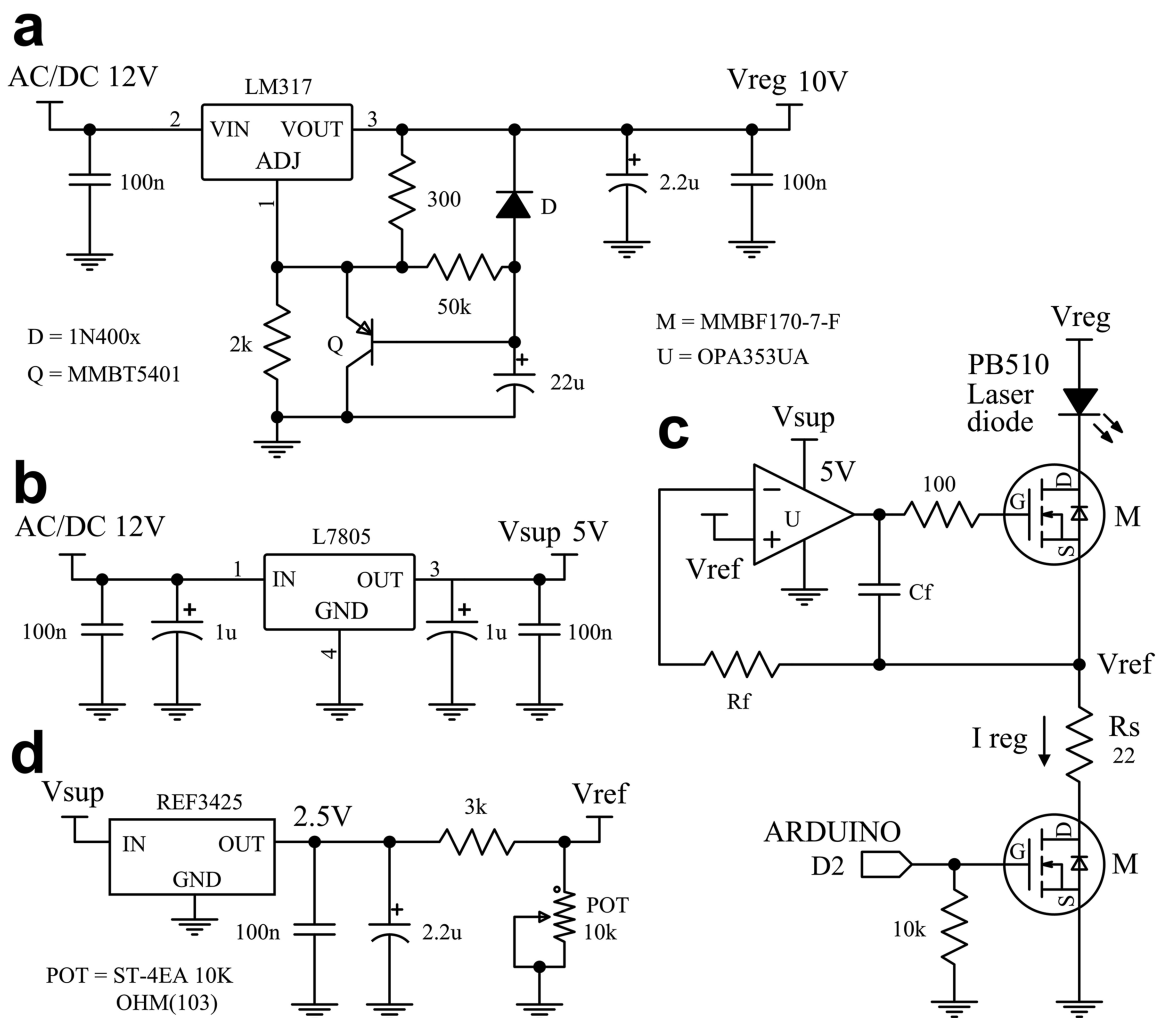


FIG. 9. Schematic of the laser driver supplied by the 12 AC/DC converter. (a) Current source with voltage regulation and a soft-start circuit. (b) Voltage regulation for the 5 V supply voltages of the op-amp and voltage reference. (c) Switched current regulator controlled by Arduino Uno. (d) Voltage reference to adjust the regulated current.

potentiometer. Figure 9(b) shows the 5 V voltage regulation to supply the OPA353UA and the REF3425.

The current pulses are generated by switching the current with a second MOSFET controlled by the digital pin D2 of Arduino Uno. The feedback capacitor C_f and resistor R_f are optional to adjust possible overshooting and the on/off delay of the pulses. The voltage V_{reg} is chosen to have $V_{reg} > V_d + V_{ref}$, where V_d is the operating voltage of the laser diode. We chose $V_{reg} \approx 10$ V to satisfy the previous condition and minimize the voltage in excess dissipated through the MOSFET and sense resistor. For our measurements, we used regulated currents in a range of 40–60 mA.

APPENDIX B: RF AMPLIFICATION

The RF signal generated by the DDS is controlled by two amplification modules made of SMD components on PCB. The first module is constituted by a buffer op-amp (OPA353UA, Texas Instruments) to match a $50\ \Omega$ load, as shown in Fig. 10(a). IOUT is a high impedance current source at the output of the DDS coupled to a $200\ \Omega$ load. The output voltage in a range of 0–600 mV is controlled by a potentiometer and AC coupled to the op-amp by a capacitor. The RF voltage is shifted at half of the power supply voltage and doubled in amplitude. Then, the voltage is coupled to an output $50\ \Omega$ resistor for impedance matching purposes and AC-coupled to the output by a capacitor.

In the second module, the signal is amplified by an RF amplifier (SPF5189, Quorvo) for a maximum output power of 23 dBm at a frequency of 2 MHz. The RF amplifier is modified from a commercial module for the operation at a frequency <10 MHz by using input and output capacitors of $2.2\ \mu\text{F}$ and a choke inductor of $220\ \mu\text{H}$ to isolate the power supply from the RF amplifier, as shown in Fig. 10(c). The amplifier is followed by a combiner with a blocking inductor and capacitor for the MW and RF fields, respectively, as shown in Fig. 10(d). The combiner is a planar bias-tee in a grounded coplanar waveguide on PCB, with SMD components installed on the central line.

The RF power at the output of the combiner as a function of the AC voltage V_{AC} and the frequency of the DDS is shown in Figs. 10(b) and 10(e). The RF power at the output of the combiner as a function of the frequency of the DDS is shown in Fig. 10(e). The RF power of the fundamental mode of a sine wave measured at the maximum amplitude of $V_{AC} = 536$ mV is nearly flat for frequencies below 8 MHz, making it suitable for the experiment of multifrequency excitation with our portable system. The output of the DDS is not filtered and contains higher order harmonics.

APPENDIX C: LIST OF MATERIALS

The main parts used for the construction of the portable setup are listed in Table I. The diamond sample is not included in the list. The additional parts to perform the experiments of multifrequency excitation of the electron spin are listed in Table II.

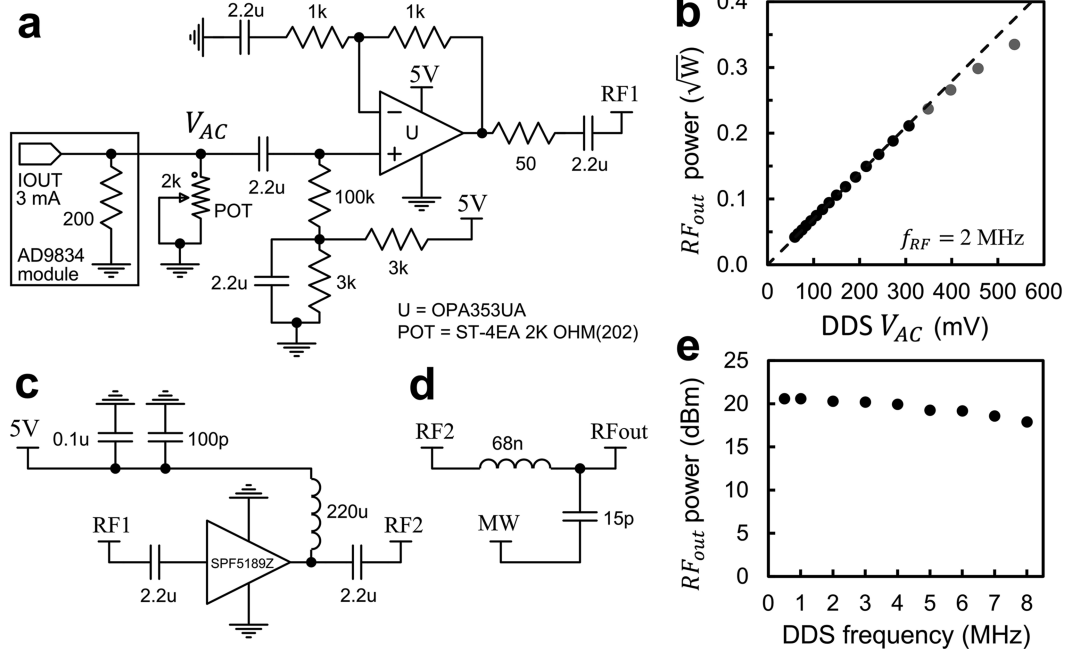


FIG. 10. (a) Schematic of the $50\ \Omega$ buffer module with a control of the RF voltage. (b) RF power at the output of the combiner as a function of the DDS AC amplitude V_{AC} at a frequency of 2 MHz. (c) Schematic of the RF amplifier module. (d) Schematic of the combiner of RF and MW pulses. Maximum RF power at the output of the combiner as a function of the DDS frequency for $V_{AC} = 536$ mV.

TABLE I. List of the main parts to assemble the portable setup. Basic SMD lumped components, such as resistors, capacitors, and inductors, are not included. The “custom PCB” indicates a part that has been installed on a customized PCB module.

Part number	Custom PCB	Store of purchase	Price (JPY)	Description
Arduino Uno		Amazon	2990	Microcontroller
USB 2.0 A/B		Amazon	725	USB cable
Succul GPE006D-060100-6		Amazon	690	6 V AC/DC converter
Succul GPE006D-120050-6		Amazon	798	12 V AC/DC converter
Succul GPE018G-150100-6		Amazon	980	15 V AC/DC converter
MB23-10-40		Misumi	3593	Al setup box
A5052P-SP6F-BA-NNN		Misumi Meviy	8330	Custom Al plate as sample holder
Neodymium magnet N35		Misumi	2242	54.7° magnet support
SDSAJ20		Amazon	(10 pcs) 1000	3 × 20∅ mm ²
LRDDG-AS		Misumi	960	Collar to hold the laser cylinder
FRDOS-D10-L40-WMC3		Misumi	2220	Bracket to hold the collar
M524 (Kyuuhoukinzoku)		Misumi	3680	SUS rods
Custom PCBs ^a		JLCPCB	~500–1000	Perforated Al sheet
TQP7M9103		Mouser	12 587	Home-built modules
TQP3M9009		Amazon	1989	MW amplifier (module)
SPF5189z		Amazon	1339	MW amplifier (module)
ADF4351		Amazon	4039	MW synthesizer (module)
HMC284AMS8GE ^b	○	Misumi	1034	MW switch module
E197VFF		Mouser	11 500	MW isolator
ADM7150ARDZ-5.0	○	RS components	(4 pcs) 4464	MW low noise regulators
ADM7160AUJZ-3.3	○	RS components	227	MW low noise regulators
Laser driver PCB	○	JLCPCB		Custom design
REF3425IDBVR	○	Misumi	749	Voltage reference
ST-4EA 10K OHM(103)	○	Misumi	(10 pcs) 560	1 turn SMD potentiometer
MMBF170-7-F (2 pcs)	○	Misumi	420	High speed MOSFET
OPA353UA	○	Misumi	239	Operational amplifier
Laser driver ICs	○	JLCPCB	~1500	Lumped components and regulators
PLT3 510 (TO38)		RS components	2625	Laser diode
CAY033		Thorlabs	1732	Aspheric lens
CAX183		Thorlabs	1732	Aspheric lens
FWZAN-D20-V7.5-P4.5-H16.5-T18.5		Misumi	830	Laser cylinder
FTCLAN-V3.5-D7.5-H20-T3-L10		Misumi	590	Laser cylinder lid
FWSAA-D7.5-V2.6-T2		Misumi	410	Collar to hold laser diode
FWSSSH-D7.5-V5.5-T1.1		Misumi	390	1.1 mm spacer to adjust the beam collimation
BPW 34 S-Z	○	RS components	(5 pcs) 1079	SMT photodiode
SCHOTT RG630		Edmund optics	3250	Absorptive longpass filter
5CGA-630		Edmund optics	4800	Reflective longpass filter
Integrator and supply PCB module	○	JLCPCB		Custom design
IVC102	○	RS components	1165	Switched integrator
LTC3260	○	RS components	1018	Integrator’s low noise power supply ±12 V
BAT54SWT1G	○	RS components	125	ADC protection diode
YFFSFDC Y45		Amazon	(2 pcs) 599	RF cable, RG316 SMA male–male 10 cm
BOOBRIE RC-3952-MD		Amazon	(2 pcs) 901	RF cable, RG316 SMA male–male 15 cm
Uxcell A11053100ux0317		Amazon	(5 pcs) 679	RF connector, PCB mount SMA female
eBayson RF-SMA-105-5JP		Amazon	(5 pcs) 799	RF connector, SMA male–male

TABLE I. (Continued.)

Part number	Custom PCB	Store of purchase	Price (JPY)	Description
132360 amphenol RF ^c		RS components	(2 pcs) 1398	RF coaxial termination, 50 Ω SMA
ELEGOO JP-EL-CP-004		Amazon	(120 pcs) 990	Jumper wires
Quilu qilun4doa86gyb		Amazon	(100 pcs) 889	Nylon hex spacers M3 × 15 mm
Uxcell A16051100ux1000		Amazon	(100 pcs) 841	Nylon screws M3 × 6 mm
Keyestudio KS0322		Amazon	(10 pcs) 1499	Arduino Uno prototype board for soldering cables
Total cost (JPY)			98 861	
Total cost (USD) ^d			~900	

^a200 × 200 mm² board on a 1.6 mm thick FR4 substrate. The cost may vary for SMT assembly and other PCB thickness.

^bModule assembled with the parts recommended in the datasheet. A dual inverter (74HCT2G04 GW, 125) is used to have an output on the port RF2 for logic high.

^cTermination for the RF1 port of the MW switch and unused output of the MW synthesizer.

^dCalculated with an average rate on July 2021.

TABLE II. List of the optional parts for the experiments of multifrequency excitation. Basic SMD lumped components, such as resistors, capacitors, and inductors, are not included.

Part number	Store of purchase	Price (JPY)	Description
AD9834	Strawberry Linux Co., Ltd.	2380	Direct digital synthesizer (module)
OPA353UA	Misumi	239	Operational amplifier
SPF5189 ^a	Amazon	1339	RF amplifier (module)
ST-4EA 2K	Misumi	(10 pcs) 560	SMD potentiometer
Custom PCBs ^b	JLCPCB	~500–1000	Home-built modules
Uxcell A11053100ux0317	Amazon	(5 pcs) 679	RF connector, PCB mount SMA female
Total cost (JPY)		6197	
Total cost (USD) ^c		~56	

^aA commercial module modified to work at RF.

^bBuffer module and RF/MW combiner realized on a 1.6 mm thick PCB with SMT assembly service.

^cCalculated with an average rate on July 2021.

REFERENCES

- H. Zhang, C. Belvin, W. Li, J. Wang, J. Wainwright, R. Berg, and J. Bridger, “Little bits of diamond: Optically detected magnetic resonance of nitrogen-vacancy centers,” *Am. J. Phys.* **86**(3), 225–236 (2018).
- E. V. Levine, M. J. Turner, P. Kehayias, C. A. Hart, N. Langellier, R. Trubko, D. R. Glenn, R. R. Fu, and R. L. Walsworth, “Principles and techniques of the quantum diamond microscope,” *Nanophotonics* **8**(11), 1945–1973 (2019).
- V. K. Sewani, H. H. Vallabhapurapu, Y. Yang, H. R. Firgau, C. Adambukulam, B. C. Johnson, J. J. Pla, and A. Laucht, “Coherent control of NV[−] centers in diamond in a quantum teaching lab,” *Am. J. Phys.* **88**(12), 1156–1169 (2020).
- D. Misonou, K. Sasaki, S. Ishizu, Y. Monnai, K. M. Itoh, and E. Abe, “Construction and operation of a tabletop system for nanoscale magnetometry with single nitrogen-vacancy centers in diamond,” *AIP Adv.* **10**(2), 025206 (2020).
- D. Kim, M. I. Ibrahim, C. Foy, M. E. Trusheim, R. Han, and D. R. Englund, “A CMOS-integrated quantum sensor based on nitrogen-vacancy centres,” *Nat. Electron.* **2**(7), 284–289 (2019).
- A. Kuwahata, T. Kitaizumi, K. Saichi, T. Sato, R. Igarashi, T. Ohshima, Y. Masuyama, T. Iwasaki, M. Hatano, F. Jelezko *et al.*, “Magnetometer with nitrogen-vacancy center in a bulk diamond for detecting magnetic nanoparticles in biomedical applications,” *Sci. Rep.* **10**(1), 2483 (2020).
- F. M. Stürner, A. Brenneis, T. Buck, J. Kassel, R. Röller, T. Fuchs, A. Savitsky, D. Suter, J. Grimmel, S. Hengesbach *et al.*, “Integrated and portable magnetometer based on nitrogen-vacancy ensembles in diamond,” *Adv. Quantum Technol.* **4**(4), 2000111 (2021).
- D. Le Sage, L. M. Pham, N. Bar-Gill, C. Belthangady, M. D. Lukin, A. Yacoby, and R. L. Walsworth, “Efficient photon detection from color centers in a diamond optical waveguide,” *Phys. Rev. B* **85**(12), 121202 (2012).
- Z. Ma, S. Zhang, Y. Fu, H. Yuan, Y. Shi, J. Gao, L. Qin, J. Tang, J. Liu, and Y. Li, “Magnetometry for precision measurement using frequency-modulation microwave combined efficient photon-collection technique on an ensemble of nitrogen-vacancy centers in diamond,” *Opt. Express* **26**(1), 382–390 (2018).
- F. M. Stürner, A. Brenneis, J. Kassel, U. Wostradowski, R. Röller, T. Fuchs, K. Nakamura, H. Sumiya, S. Onoda, J. Isoya, and F. Jelezko, “Compact integrated magnetometer based on nitrogen-vacancy centres in diamond,” *Diamond Relat. Mater.* **93**, 59–65 (2019).
- J. L. Webb, J. D. Clement, L. Troise, S. Ahmadi, G. J. Johansen, A. Huck, and U. L. Andersen, “Nanotesla sensitivity magnetic field sensing using a compact diamond nitrogen-vacancy magnetometer,” *Appl. Phys. Lett.* **114**(23), 231103 (2019).
- D. Zheng, Z. Ma, W. Guo, L. Niu, J. Wang, X. Chai, Y. Li, Y. Sugawara, C. Yu, Y. Shi *et al.*, “A hand-held magnetometer based on an ensemble of nitrogen-vacancy centers in diamond,” *J. Phys. D: Appl. Phys.* **53**(15), 155004 (2020).
- R. Hošák and M. Ježek, “Arbitrary digital pulse sequence generator with delay-loop timing,” *Rev. Sci. Instrum.* **89**(4), 045103 (2018).
- C. A. Michal, “A low-cost spectrometer for NMR measurements in the Earth’s magnetic field,” *Meas. Sci. Technol.* **21**(10), 105902 (2010).
- K. Yubonhat, W. Youngdee, S. Chinwong, and N. Saowadee, “A low-cost Arduino-based NMR console,” *J. Phys.: Conf. Ser.* **1380**, 012012 (2019).

- ¹⁶E. D. C. Sánchez, A. R. Pessoa, A. M. Amaral, and L. de S. Menezes, "Microcontroller-based magnetometer using a single nitrogen-vacancy defect in a nanodiamond," *AIP Adv.* **10**(2), 025323 (2020).
- ¹⁷A. Doll, "Pulsed and continuous-wave magnetic resonance spectroscopy using a low-cost software-defined radio," *AIP Adv.* **9**(11), 115110 (2019).
- ¹⁸X. Qin, W. Zhang, L. Wang, Y. Zhao, Y. Tong, X. Rong, and J. Du, "An FPGA-based hardware platform for the control of spin-based quantum systems," *IEEE Trans. Instrum. Meas.* **69**(4), 1127–1139 (2020).
- ¹⁹C. D. Aiello, D. D. Awschalom, H. Bernien, T. Brower, K. R. Brown, T. A. Brun, J. R. Caram, E. Chitambar, R. Di Felice, K. M. Edmonds *et al.*, "Achieving a quantum smart workforce," *Quantum Sci. Technol.* **6**(3), 030501 (2021).
- ²⁰A. Asfaw, A. Blais, K. R. Brown, J. Candelaria, C. Cantwell, L. D. Carr, J. Combes, D. M. Debroy, J. M. Donohue, S. E. Economou *et al.*, "Building a quantum engineering undergraduate program," *IEEE Trans. Educ.* **65**, 220 (2022).
- ²¹EasyEDA (last accessed January 5, 2021), <https://easyceda.com/>.
- ²²K. Sasaki, Y. Monnai, S. Saijo, R. Fujita, H. Watanabe, J. Ishi-Hayase, K. M. Itoh, and E. Abe, "Broadband, large-area microwave antenna for optically detected magnetic resonance of nitrogen-vacancy centers in diamond," *Rev. Sci. Instrum.* **87**(5), 053904 (2016).
- ²³G. Mariani, S. Nomoto, S. Kashiwaya, and S. Nomura, "System for the remote control and imaging of MW fields for spin manipulation in NV centers in diamond," *Sci. Rep.* **10**(1), 4813 (2020).
- ²⁴Arduino UNO Port Manipulation (last accessed January 5, 2021), <https://www.arduino.cc/en/Reference/PortManipulation>.
- ²⁵Ivc102 datasheet (last accessed January 5, 2021), <https://www.ti.com/lit/ds/symlink/ivc102.pdf>.
- ²⁶Atmel Corporation, AVR121: Enhancing ADC resolution by oversampling, Atmel Corporation, 2005, <http://ww1.microchip.com/downloads/en/appnotes/doc8003.pdf>.
- ²⁷M. Mrózek, D. Rudnicki, P. Kehayias, A. Jarmola, D. Budker, and W. Gawlik, "Longitudinal spin relaxation in nitrogen-vacancy ensembles in diamond," *EPJ Quantum Technol.* **2**, 22 (2015).
- ²⁸A. Jarmola, V. M. Acosta, K. Jensen, S. Chemerisov, and D. Budker, "Temperature- and magnetic-field-dependent longitudinal spin relaxation in nitrogen-vacancy ensembles in diamond," *Phys. Rev. Lett.* **108**(19), 197601 (2012).
- ²⁹L. Childress, M. V. Gurudev Dutt, J. M. Taylor, A. S. Zibrov, F. Jelezko, J. Wrachtrup, P. R. Hemmer, and M. D. Lukin, "Coherent dynamics of coupled electron and nuclear spin qubits in diamond," *Science* **314**(5797), 281–285 (2006).
- ³⁰E. Bauch, S. Singh, J. Lee, C. A. Hart, J. M. Schloss, M. J. Turner, J. F. Barry, L. M. Pham, N. Bar-Gill, S. F. Yelin *et al.*, "Decoherence of ensembles of nitrogen-vacancy centers in diamond," *Phys. Rev. B* **102**(13), 134210 (2020).
- ³¹P. L. Stanwix, L. M. Pham, J. R. Maze, D. Le Sage, T. K. Yeung, P. Cappellaro, P. R. Hemmer, A. Yacoby, M. D. Lukin, and R. L. Walsworth, "Coherence of nitrogen-vacancy electronic spin ensembles in diamond," *Phys. Rev. B* **82**(20), 201201 (2010).
- ³²L. Childress and J. McIntyre, "Multifrequency spin resonance in diamond," *Phys. Rev. A* **82**(3), 033839 (2010).
- ³³S. Rohr, E. Dupont-Ferrier, B. Pigeau, P. Verlot, V. Jacques, and O. Arcizet, "Synchronizing the dynamics of a single nitrogen vacancy spin qubit on a parametrically coupled radio-frequency field through microwave dressing," *Phys. Rev. Lett.* **112**(1), 010502 (2014).
- ³⁴A. P. Saiko, R. Fedaruk, and S. A. Markevich, "Suppression of electron spin decoherence in Rabi oscillations induced by an inhomogeneous microwave field," *J. Magn. Reson.* **290**, 60–67 (2018).
- ³⁵T. Tashima, H. Morishita, and N. Mizuochi, "Experimental demonstration of two-photon magnetic resonances in a single-spin system of a solid," *Phys. Rev. A* **100**(2), 023801 (2019).
- ³⁶J.-M. Cai, B. Naydenov, R. Pfeiffer, L. P. McGuinness, K. D. Jahnke, F. Jelezko, M. B. Plenio, and A. Retzker, "Robust dynamical decoupling with concatenated continuous driving," *New J. Phys.* **14**(11), 113023 (2012).
- ³⁷D. Farfurnik, N. Aharon, I. Cohen, Y. Hovav, A. Retzker, and N. Barr-Gill, "Experimental realization of time-dependent phase-modulated continuous dynamical decoupling," *Phys. Rev. A* **96**(1), 013850 (2017).
- ³⁸G. Wang, Y.-X. Liu, and P. Cappellaro, "Observation of the high-order Mollow triplet by quantum mode control with concatenated continuous driving," *Phys. Rev. A* **103**(2), 022415 (2021).
- ³⁹M. Loretz, T. Rosskopf, and C. L. Degen, "Radio-frequency magnetometry using a single electron spin," *Phys. Rev. Lett.* **110**(1), 017602 (2013).
- ⁴⁰Y. Liu, F. Kong, F. Shi, and J. Du, "Detection of radio-frequency field with a single spin in diamond," *Sci. Bull.* **61**(14), 1132–1137 (2016).
- ⁴¹S. Nomura, K. Kaida, H. Watanabe, and S. Kashiwaya, "Near-field radio-frequency imaging by spin-locking with a nitrogen-vacancy spin sensor," *J. Appl. Phys.* **130**(2), 024503 (2021).
- ⁴²J. Meinel, V. Vorobyov, B. Yavkin, D. Dasari, H. Sumiya, S. Onoda, J. Isoya, and J. Wrachtrup, "Heterodyne sensing of microwaves with a quantum sensor," *Nat. Commun.* **12**(1), 2737 (2021).
- ⁴³O. R. Opaluch, N. Oshnik, R. Nelz, and E. Neu, "Optimized planar microwave antenna for nitrogen vacancy center based sensing applications," *Nanomaterials* **11**(8), 2108 (2021).
- ⁴⁴K. Herb, J. Zopes, K. S. Cujia, and C. L. Degen, "Broadband radio-frequency transmitter for fast nuclear spin control," *Rev. Sci. Instrum.* **91**(11), 113106 (2020).
- ⁴⁵K. Bayat, J. Choy, M. Farrokh Baroughi, S. Meesala, and M. Loncar, "Efficient, uniform, and large area microwave magnetic coupling to NV centers in diamond using double split-ring resonators," *Nano Lett.* **14**(3), 1208–1213 (2014).
- ⁴⁶A. P. Saiko, R. Fedaruk, and S. A. Markevich, "Relaxation, decoherence, and steady-state population inversion in qubits doubly dressed by microwave and radiofrequency fields," *J. Phys. B: At. Mol. Opt. Phys.* **47**(15), 155502 (2014).
- ⁴⁷D. P. DiVincenzo, "The physical implementation of quantum computation," *Fortschr. Phys.* **48**(9–11), 771–783 (2000).
- ⁴⁸J. Teissier, A. Barfuss, P. Appel, E. Neu, and P. Maletinsky, "Strain coupling of a nitrogen-vacancy center spin to a diamond mechanical oscillator," *Phys. Rev. Lett.* **113**(2), 020503 (2014).
- ⁴⁹A. K. Dmitriev, H. Y. Chen, G. D. Fuchs, and A. K. Vershovskii, "Dual-frequency spin-resonance spectroscopy of diamond nitrogen-vacancy centers in zero magnetic field," *Phys. Rev. A* **100**(1), 011801 (2019).
- ⁵⁰S. Saijo, Y. Matsuzaki, S. Saito, T. Yamaguchi, I. Hanano, H. Watanabe, N. Mizuochi, and J. Ishi-Hayase, "AC magnetic field sensing using continuous-wave optically detected magnetic resonance of nitrogen-vacancy centers in diamond," *Appl. Phys. Lett.* **113**(8), 082405 (2018).
- ⁵¹J. F. Barry, M. J. Turner, J. M. Schloss, D. R. Glenn, Y. Song, M. D. Lukin, H. Park, and R. L. Walsworth, "Optical magnetic detection of single-neuron action potentials using quantum defects in diamond," *Proc. Natl. Acad. Sci. U. S. A.* **113**(49), 14133–14138 (2016).
- ⁵²H. A. R. El-Ella, S. Ahmadi, A. M. Wojciechowski, A. Huck, and U. L. Andersen, "Optimised frequency modulation for continuous-wave optical magnetic resonance sensing using nitrogen-vacancy ensembles," *Opt. Express* **25**(13), 14809–14821 (2017).